where $g(\mathbf{r},\mathbf{r}') = \dfrac{e^{-jk|\mathbf{r}-\mathbf{r}'|}}{4\pi|\mathbf{r}-\mathbf{r}'|}$ is the scalar Green function, $\mathbf{J}_v$ is the volumetric polarization current, and the permittivity and permeability in free space are $\varepsilon_0$ and $\mu_0$, respectively. The position-dependent relative permittivity of the inhomogeneous solar cell is $\varepsilon_r(\mathbf{r})$, and $\mathbf{E}^i(\mathbf{r})$ is the incident field.

The Schaubert-Wilton-Glisson (SWG) basis functions are employed to expand the volumetric polarization currents. Then the matrix equation can be obtained by using the Galerkin's test method [22].

$$
\begin{aligned}
&(j\omega)^2\mu_0\int_{v_m} dv_m \mathbf{f}_m^v(\mathbf{r})\int_{v_n'} \kappa_n(\mathbf{r}')\mathbf{f}_n^v(\mathbf{r}')\cdot g(\mathbf{r},\mathbf{r}')dv_n' \\
&+\frac{1}{\varepsilon_0}\int_{v_m} dv_m \nabla\cdot\mathbf{f}_m^v(\mathbf{r})\int_{v_n'} \kappa_n(\mathbf{r}')\nabla'\cdot\mathbf{f}_n^v(\mathbf{r}')\cdot g(\mathbf{r},\mathbf{r}')dv_n' \\
&-\frac{1}{\varepsilon_0}\int_{v_m} dv_m \nabla\cdot\mathbf{f}_m^v(\mathbf{r})\int_{v_n'} \left(\mathbf{f}_m^v(\mathbf{r}')\nabla'\kappa_n(\mathbf{r}')\right)\cdot g(\mathbf{r},\mathbf{r}')dv_n' \\
&-\frac{1}{\varepsilon_0}\int_{\Omega_m} \mathbf{f}_m^v(\mathbf{r})\cdot\mathbf{n}d\Omega_m\int_{v_n'} \kappa_n(\mathbf{r}')\nabla'\cdot\mathbf{f}_n^v(\mathbf{r}')\cdot g(\mathbf{r},\mathbf{r}')dv_n' \\
&+\frac{1}{\varepsilon_0}\int_{\Omega_m} \mathbf{f}_m^v(\mathbf{r})\cdot\mathbf{n}d\Omega_m\int_{v_n'} \left(\mathbf{f}_m^v(\mathbf{r}')\nabla'\kappa_n(\mathbf{r}')\right)\cdot g(\mathbf{r},\mathbf{r}')dv_n' \\
&+\int_{v_m} dv_m \mathbf{f}_m^v(\mathbf{r})\frac{1}{\varepsilon_n(\mathbf{r}')}\mathbf{f}_m^v(\mathbf{r}') = \int_{v_m}\mathbf{E}^i(\mathbf{r})\cdot\mathbf{f}_m^v(\mathbf{r})dv_m
\end{aligned}
\tag{2}
$$

where $\kappa_n(\mathbf{r}') = \dfrac{\varepsilon_0\varepsilon_r(\mathbf{r}')-\varepsilon_0}{\varepsilon_0\varepsilon_r(\mathbf{r}')}$, $\mathbf{f}^v$ is the SWG basis function, and $\Omega$ stands for the outside interface of the tetrahedron $v$.

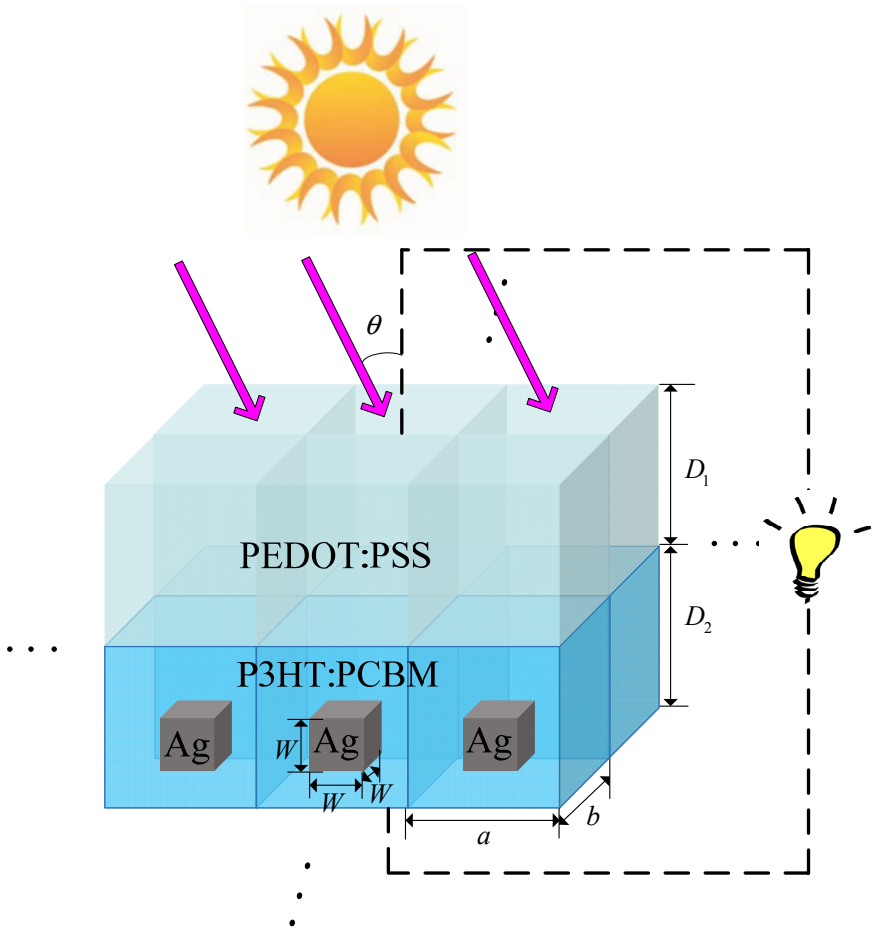


Fig. 1. The schematic of the plasmonic OSC. Periodic silver (Ag) NP array is embedded at the active layer (P3HT:PCBM) of the OSCs. The PEDOT:PSS layer is a spacer layer. The device is illuminated by sunlight with an incident angle of $\theta$. The geometry of the device structure is: The cell size is $a \times b \times D_1$ for the PEDOT:PSS domain, $a \times b \times D_2$ for the P3HT:PCBM domain and $W \times W \times W$ for the Ag domain.

### 2.2 Two-dimensional periodic Green's functions

Figure 1 shows the schematic of the plasmonic OSC, which is periodic along the $x$ and $y$ directions. The lattice constants along the $x$ and $y$ axes are $a$ and $b$, respectively. The incident angle of the sunlight is set to be $\theta$. Then the two-dimensional periodic Green's functions (PGF) can be derived as [19-20]

$$g_p = \sum \frac{e^{-jk_0 R_{mn}}}{4\pi R_{mn}} e^{j(k_x^i ma + k_y^i nb)} \tag{3}$$

where $k_x^i = k_0 \sin\theta\cos\varphi$ and $k_y^i = k_0 \sin\theta\sin\varphi$. According to the Bloch-Floquet theorem, $k_x^i$ and $k_y^i$ are the phase shifts between adjacent cells along the $x$ and $y$ directions, and $(\theta, \varphi)$ is the incident angle. $R_{mn}$ is the distance between the source and observation points, i.e.

$$R_{mn} = \sqrt{(x - x' + ma)^2 + (y - y' + nb)^2 + (z - z')^2} \tag{4}$$

It should be noted that the calculation of the periodic Green's functions can be accelerated by the Ewald's method [21, 27,28]. The Ewald's method splits the periodic Green's functions into a sum of the spatial and spectral series. More specifically, the spatial series can be calculated with the Ewald identity [21] and the spectral series can be obtained by using the Poisson summation formula [25]. In this way, both the spatial and spectral series achieve good convergence.

### *2.3. Domain decomposition-based diagonal block preconditioner*

As shown in Fig. 1, without loss of generality, there are three types of materials for a unit cell of the plasmonic OSC, including the spacer layer (PEDOT:PSS) domain, active layer (P3HT:PCBM) domain and plasmonic NP (Ag) domain. The cell size is $a \times b \times D_1$ for the PEDOT:PSS domain, $a \times b \times D_2$ for the P3HT:PCBM domain and $W \times W \times W$ for the Ag domain. Then the impedance matrix can be split into small submatrices with respect to different material domains. Thus, the matrix equation can be rewritten as

$$\begin{bmatrix} A_{11} & A_{12} & A_{13} \\ A_{21} & A_{22} & A_{23} \\ A_{31} & A_{32} & A_{33} \end{bmatrix} \begin{bmatrix} x_1 \\ x_2 \\ x_3 \end{bmatrix} = \begin{bmatrix} b_1 \\ b_2 \\ b_3 \end{bmatrix} \tag{5}$$

where $A_{ii}\ (i = 1,2,3)$ describes the self-interaction of the $i$-th domain, and $A_{ij}\ (i = 1,2,3, j = 1,2,3)$ represents the mutual interaction between the $i$-th and $j$-th domains.

Considering the convergence will become worse for different dispersive media, we use the block diagonal preconditioner to handle each dispersive medium region. Moreover, the block diagonal preconditioner is easy to be implemented and has a good performance. Then, the diagonal block preconditioner is respectively constructed for $A_{11}, A_{22}, A_{33}$ as follows:

$$\begin{bmatrix} A_{11}^{-1} & & \\ & A_{22}^{-1} & \\ & & A_{33}^{-1} \end{bmatrix} \begin{bmatrix} A_{11} & A_{12} & A_{13} \\ A_{21} & A_{22} & A_{23} \\ A_{31} & A_{32} & A_{33} \end{bmatrix} \begin{bmatrix} x_1 \\ x_2 \\ x_3 \end{bmatrix} = \begin{bmatrix} A_{11}^{-1} b_1 \\ A_{22}^{-1} b_2 \\ A_{33}^{-1} b_3 \end{bmatrix}. \tag{6}$$

Compared to Eq. (5), the convergence of the preconditioned Eq. (6) is significantly improved. Consequently, the three-dimensional full-wave analyses of the OSCs incorporating metallic NPs can be numerically implemented with a high efficiency.

## 3. Numerical results

All the numerical results are produced by the computer of Intel Xeon E7-4850 CPU equipped with 8GB RAM. The incident plane waves with the wavelengths ranging from 400 nm to 800 nm are assumed as the sunlight illumination. The light absorption is defined as

$$A(\lambda) = \omega \int_v \mathrm{Im}\left(\varepsilon(\lambda, \mathbf{r})\right) \left|\mathbf{E}(\lambda, \mathbf{r})\right|^2 dv \tag{7}$$

where $\lambda$ is the wavelength, $\mathrm{Im}(\varepsilon)$ denotes the imaginary part of the complex permittivity for the active organic materials, and $\mathbf{E}$ represents the electric field at the active layer. It should be noted that the integral is only made at the active material domain of the OSC (excluding the metallic domain). Then, absorption enhancement can be obtained by dividing the light absorption of the OSC with the NPs by that of the OSC without the NPs.

In the beginning, the convergence performance of the domain decomposition-based diagonal block preconditioner is tested under the wavelength of 400 nm condition. The device

structure of the OSC is depicted in Fig. 1 and only six unit cells are shown. Ag NPs are embedded into the active layer. *W* and *a (a = b)* are chosen as 20 nm and 40 nm, respectively. And the thickness is 20 nm for the spacer layer, 60 nm for the active layer. As illustrated in Fig. 2, regarding the two-layer OSC, the convergence curves of the generalized minimal residual (GMRES) iteration method [23] with and without the preconditioner are given. Moreover, Fig. 3 depicts the relative errors of the current coefficients, which can be defined as

$$\varepsilon_{re} = \frac{\left\| J_{Pre} - J_{No-pre} \right\|_2}{\left\| J_{No-pre} \right\|_2} \tag{8}$$

where $J_{Pre}$ and $J_{No-pre}$ are the current coefficients obtained with and without the preconditioner, respectively.

As shown in Fig. 3, the relative errors of all the unknowns are less than 12%. It can be concluded that the computational efficiency can be improved with encouraging accuracy by using the proposed preconditioner technique.

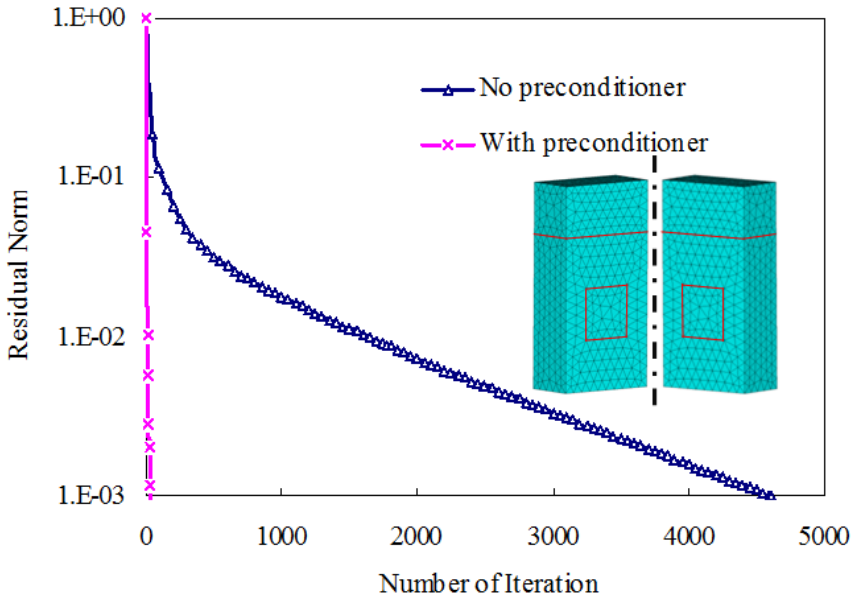


Fig. 2. Residual convergence curves of the GMRES iteration for the plasmonic OSC. The cross and triangle lines are the convergence results for the VIE methods with and without the preconditioners, respectively.

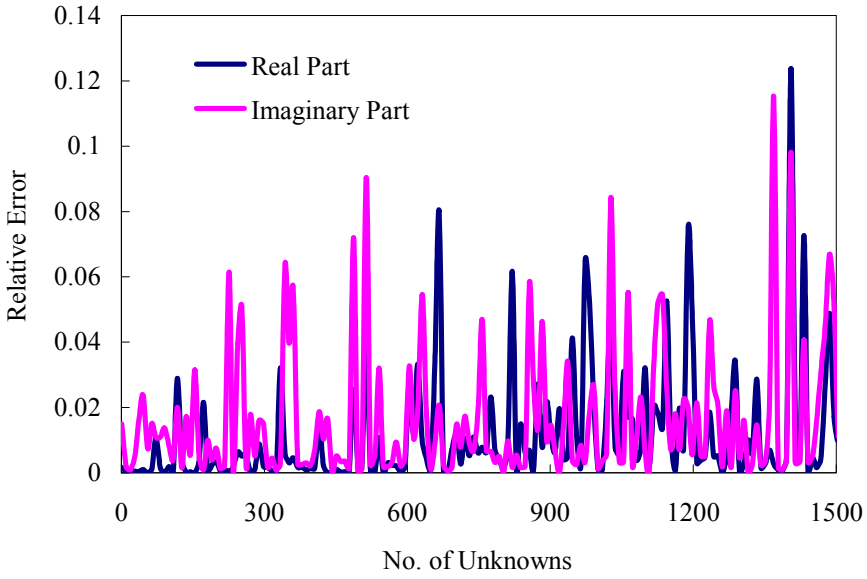


Fig. 3. Relative errors of the complex current coefficients by the VIE methods with and without the preconditioners.

Then we optimize the lattice constant *a (a = b)* to maximize the absorption enhancement with $W = 40$ nm at the perpendicular incidence. The thickness of the active layer is 60 nm and that of the spacer layer is 20 nm. As shown in Fig. 4, the absorption spectra of the OSC are demonstrated as a function of the lattice constant. As the lattice constant decreases, the plasmonic coupling and hybridization between adjacent Ag NPs become stronger. The largest absorption enhancement factor up to 32 can be obtained for $a = 60$ nm. However, a very small lattice constant (a = 50 nm) reduces the volume of active materials (P3HT:PCBM) significantly; and thus lowers the optical absorption. The absorption spectra show three peaks around 500 nm, 600 nm, and 750 nm as depicted in Fig. 4. The waveguide mode (at the peak 1, E-field is bound between the top and bottom interfaces of the P3HT:PCBM layer), blue-shifted transverse plasmonic mode (at the peak 2), and red-shifted longitudinal plasmonic mode (at the peak 3) are excited from short wavelengths to long wavelengths, respectively. The strongest enhancement is gained by the longitudinal plasmonic mode with the resonating wavelength of 750 nm. To further understand the optical enhancement mechanisms, the wavelength-dependent absorption profiles at the active layer are illustrated in Fig. 5 with $a = 60$ nm. Although the Ag NPs show large metallic loss, the plasmonic near fields still penetrate into the active layer and absorbed by organic active materials.

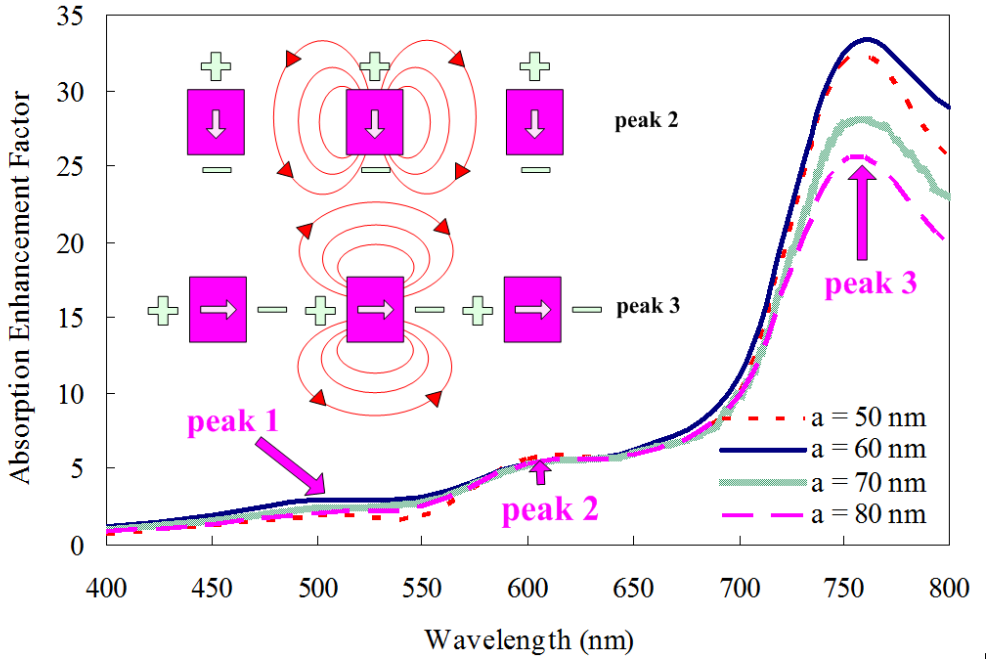


Fig. 4. Absorption spectra of the plasmonic solar cell as a function of the lattice constant. The absorption is calculated only from the P3HT:PCBM active material. The arrows denote the resonance peaks. The peaks 1, 2, 3 are related to the excited waveguide mode, transverse plasmonic mode, and longitudinal plasmonic mode. The coupling mechanisms of the transverse mode (peak 2) and longitudinal mode (peak 3) are shown in the inset.

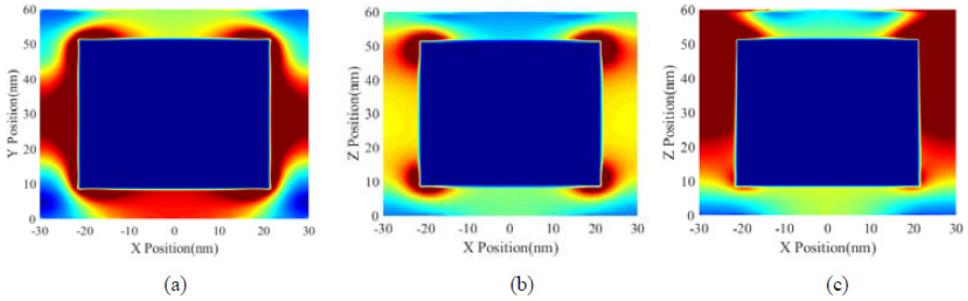


Fig. 5. Absorption profiles of active layer at the three resonance wavelengths of Fig. 4. The lattice constant is a = 60 nm. (a) $\lambda = 500$ nm (peak 1); (b) $\lambda = 600$ nm (peak 2); (c) $\lambda = 750$ nm (peak 3).

Finally, the performance of the OSC ($W = 40$ nm, $a = b = 60$ nm, $D_1 = 20$ nm, $D_2 = 60$ nm) is theoretically modelled over a wide range of incident angles, which is essential to the practical solar cell devices [24]. Figure 6 shows the wavelength-dependent angular response of the plasmonic OSC. The absorption enhancement factors decrease as the incident angle increases. On the longitudinal plasmon resonance wavelength (750 nm), the normalized absorption, as the incident angle increases, shows the super-Lambertian feature, i.e. it decays much slower than the ideal Lambertian absorption curve of $\cos(\theta)$. On the transverse plasmon resonance wavelength (600 nm), the absorption decays faster but still shows the super-Lambertian absorption. In contrast, on the waveguide resonance wavelength, which is off the plasmon resonance wavelengths, the angular response is more close to the ideal Lambertian curve. Thus,

the plasmonic resonances, compared to the waveguide resonance, are more insensitive to the incident angle.

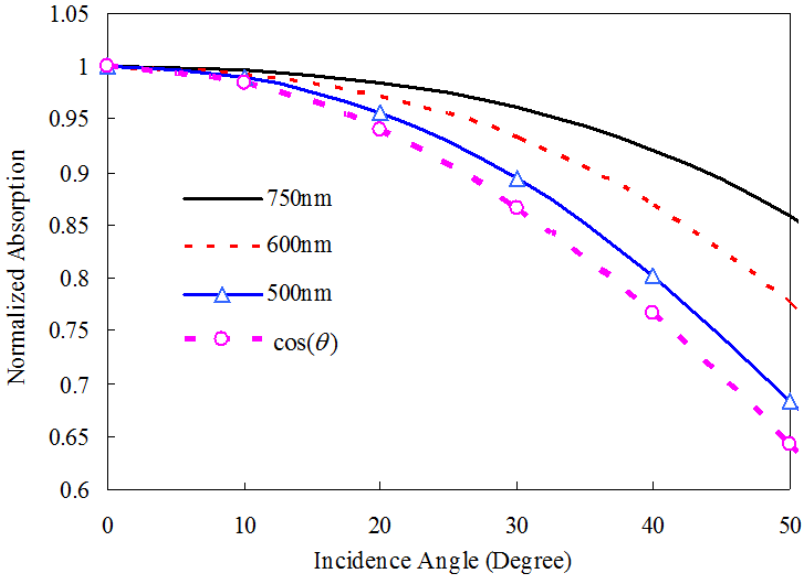


Fig. 6. Wavelength-dependent angular responses of the plasmonic solar cell. The ideal Lambertian curve is given for comparisons. The 500 nm, 600 nm, and 750 nm correspond to the three resonance wavelengths of Fig. 4.

## 4. Conclusion

A volumetric method of moments is proposed as a full-wave solution to model thin-film solar cells incorporating periodic plasmonic structures. By introducing the two-dimensional periodic Green's functions, the calculation is only needed to be implemented in a unit cell. Therefore, the computational resources can be saved significantly. Particularly, a domain decomposition-based diagonal block preconditioner is applied at different material domains to overcome the bad convergence of impedance matrix equation caused by plasmonic effects.

Numerical examples are presented to demonstrate the efficiency of the proposed method. Most importantly, we found that the angular responses of plasmonic solar cells significantly break the Lambertian absorption limits on the plasmon resonance wavelengths but show near-Lambertian absorption off the plasmon resonance wavelengths. Our work offers a promising mathematical approach and deep physical understanding to the optical designs of nanostructured OSCs.

## Funding

Natural Science Foundation of 61701232, Jiangsu Province Natural Science Foundation of BKs20170854, the Young Elite Scientists Sponsorship Program by CAST of 2017QNRC001, the China Postdoctoral Science Foundation of 2017M620861 and 2018T110127, the Fundamental Research Funds for the central Universities of No.30917011317, and the State Key Laboratory of Millimeter Waves of K201805. The project was also supported by Thousand Talents Program for Distinguished Young Scholars of China (588020-X01801/009).

## Acknowledgment

We thank Prof. Weng Cho Chew from Purdue University for helpful discussions about theoretical details.